Experimental Characterization of Straw Jets via Image Processing Techniques

Miguel Alfonso Mendez[1,*] **and Jean-Marie Buchlin**[1]

[1]Environmental and Applied Fluid Dynamics Department, von Karman Institute for Fluid Dynamics, Rhode Saint Genèse, Belgium
[*]corresponding author: mendez@vki.ac.be

Abstract This paper presents a non-intrusive experimental technique to characterize the dense particle laden jet flow produced by straw blowers machine. These flows are often encountered in agricultural contexts for bedding, feeding or mulching applications. The experimental set up consists of a straw blower machine, a white background tarp and a color video camera filming the straw jet over a twelve meter test section, in daylight conditions. The technique is based on an image processing routine to detect and track straw particles from the video sequence. In particular, the processing combines two segmentation techniques: 1) a color segmentation, using k-means clustering in the CIElab color space and 2) an adaptive background subtraction, using Eigen-Background decomposition. For a set of four test cases, the straw jet trajectories obtained were complemented –and validated– with the measurement of straw distribution at the ground using a mesh of panels.
Keywords: Image Processing for Particle-Laden Flows, K-means Clustering Segmentation, Eigen-Background Subtraction, Straw Jets.

1 Introduction

The dispersion of straw materials from wheat, oats, barley, timothy or rye is widely used in agricultural applications such as fodder distribution or soil mulching ([1, 2, 3]). These operations are carried out with straw blower machines, which chops up to $20 tons/hours$ of straw material and casts it at distances of the order of $20-30m$. The flow produced is a complex turbulent particle-laden flow with high straw-to-air volume concentrations and high particle-to-particle interaction.

On the other hand, straw blower machines are required to be highly versatile, with performances defined in any operating condition. As no simple modeling of these flows exists, the only tool at the designers' disposal is experience, based on expensive trial and error testing. A standard test consists in operating the machine on a mesh of panels on the ground, and weight the straw distribution within a time interval. This method provides the range of the blower and the final straw dispersion. However, it is extremely time-consuming and offers no insights on the dynamics of the flow.

This paper proposes a simple and fast method to characterize the trajectory and the spreading of a straw jet using a color photo camera and a white tarp, in daylight conditions. The method is based on an image processing routine to detect and extract straw particles in a sequence of images. It can be fully automated and its robustness can be extended to the experimental characterization of others two-phase flows. The challenge of determining– and tracking– particles or flow boundaries from video records is, in fact, fundamental in the non-intrusive characterization of any multiphase flows. Different approaches are reviewed in [4, 5, 6, 7].

A common approach consists in acquiring grayscale images, threshold the dispersed phase, based on its higher intensity with respect to the background, and perform morphologic operation on the resulting binary image. These operations, based on connectivity analysis, include labeling and computation of particle centroid, equivalent diameters and displacements [8, 9, 10, 11].

The success of these methods, however, stands upon the threshold step. Specifically, in the identification of the grayscale value above which a pixel is classified as belonging to the dispersed phase –a bubble, a solid particle or any object to extract– or as belonging to the background. This classification problem is essential in any computer vision application, and is known as segmentation.

Comprehensive reviews of grayscale (monochrome) segmentation are proposed in [12, 13, 14]. These papers show how different thresholding techniques leads to different results, depending on the image histogram. It is not surprising, then, that the robustness of an image-based measurements relies on the control of the illumination to have sufficiently re-contrasted images and, ideally, with bimodal distribution histograms.

The same constraints applies for edge detection algorithms, which are often used, in experimental fluid mechanics, to track gas-liquid interfaces. Diluting fluorescent tracers on a liquid, and illuminating its interface with a laser sheet, allows to acquire highly contrasted images on which several edge detection algorithms operate accurately. Depending on the image exposure, tracers may appear either as a uniformly brighter regions or as a discrete set of particles like in Particle Image Velocimetry (PIV) acquisitions. The first configuration is used in the Level Detection and Recording (LeDaR) technique ([15, 16, 17]), in which gas-liquid interfaces are detected using image convolution with Sobel-like kernels. The second configuration is of interest in the dynamic masking algorithms for PIV measurements in two-phase flows. An example is proposed in [18], based on the Radon transform, which is a mathematical tool used for detecting linear features in *salt-and-pepper* noisy images ([19]).

Nevertheless, when experimental conditions do not allow to control the illumination, like in the case analyzed in this paper, the contrast of the images is often insufficient for any monochrome segmentation or edge extraction method. The processing method proposed in this work aims to release the constraints on the illumination and the image contrast, to allow for straw particle segmentation also in non-optimal, daylight conditions. The method requires color images, which are processed in three steps. The first step extracts straw elements based on their color properties. The second step refines the segmentation by removing static objects from the images. The third step computes the average image to detect the jet boundaries, its trajectory and spreading.

Because of the higher amount of information conveyed by color images, the number of possible segmentation approaches is higher: a color image contains several gray scale images, each of which represents a color component with respect to a color space. On the other hand, there exist many color spaces derived from the standard tristimuli Red (R), Green (G) and Blue (B), and none of them has yet been proved superior for all purposes. Comprehensive reviews on the color segmentation are proposed in [20] and [21].

Some authors use the color information to extract objects based on color homogeneity (e.g.[24, 25]). Other authors use the color information to compute a grayscale image suited for which monochrome segmentation (e.g [22, 23]). The color segmentation this work uses a combines both approaches.

The routine starts with a classification. The images acquired have a simple texture: they contain (1) straw elements on a white (2) background that has (3) dark defects, such as shadows or background tarp ripples, and (4) bright defects , such as sunlight spots. The first segmentation step consist in classifying the image pixels as belonging to one of these four clusters and extract the one containing the straw elements. The method proposed is based on k-means clustering performed on the CIE *Lab* color space, which key advantages for clustering approaches are reported in [26] and [27].

The second processing step refines the segmentation removing static objects which eventually remains after the first step. The method proposed is the adaptive Eigen-Background subtraction. Adaptive background techniques are popular in automatic video analysis, especially in video surveillance, where cameras works in time varying and non optimal light conditions. Subtraction methods consider moving objects as connected area which *significantly* differ from a reference image. This image, however, needs to be continuously adapted to compensate for all the challenges that an outdoor environments sets, such as slow illumination variation from down to dusk, camera oscillation or disruptive glare of reflected sunlight. Comprehensive review on the topic are proposed in [28] and [29].

The Eigen-background method was introduced in [30] and it is based on the assumption that moving objects are unlikely to appear in the same position at different frames and, moreover, only occupies small portions of the image. Therefore, if the video sequence is reshaped into a matrix, and decomposed into its principal components via Principal Component Analysis (PCA), the static backgrounds are to be found within the first, high energy, components, whereas the moving objects will belong to last, low energy, components.

The third step of the image processing consists in averaging the straw images, to compute the mean jet trajectory, and computing the jet edges via standard monochrome segmentation. The method proposed is Otsu's binarization, followed by a morphological filter to extract only the biggest connected area.

The three image processing steps are described in Sec.3 and the results for the test cases studied are presented and discussed in Sec.4. Test cases and experimental set up are introduced in the following section.

2 Experimental Set Up and Conditions

The experiments are conducted in a closed barn to avoid wind disturbances. The barn has windows on the roof and on the sides so that daylight illuminates the scene. The set up is sketched in Fig.1, with the reference frame used hereinafter. A $15m \times 3m$ white tarp sets the background. In the ground, a mesh of $(1 \times 1m^2)$ panels is installed, covering an area of $3 \times 16m^2$. The blower is a Kuhn Primotor 3570 , positioned 3 meters from the first raw of panel. The camera used is a Canon $EOS1100D$, with $EFS18-55mm$ objective, and it is installed on a podium at $3m$ from the ground, and $30m$ from the image plane. The field of view is about $12m$ large.

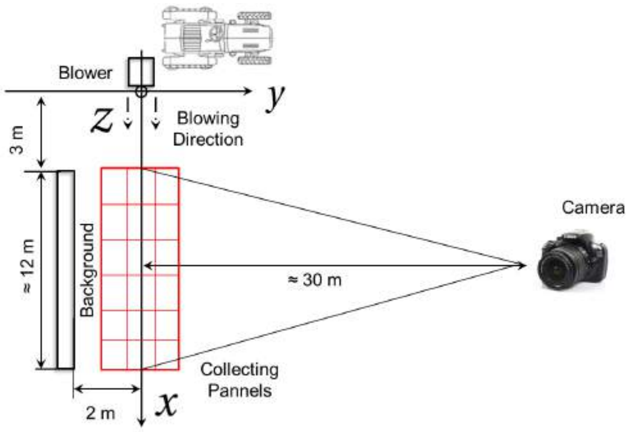

Fig. 1 Sketch of the experimental set up.

Fig.2 shows a typical calibration image. The test section is empty and a calibrator is aligned with the axis of the nozzle at the blower's outlet. The support of the calibrator indicates the location of the ground line in the local XZ plane, so the image is cropped to have $Z = 0$ in the last pixel raw.

The calibrator has a pattern of circles of $22cm$ diameter, positioned in the $Z = -0.5m$ and $Z = 0.5m$ plane. This has been used to compute the magnification factor and its uncertainty, estimated as twice the standard deviation of the circles diameter measurements in pixels. The results is $M = 2.78 \pm 0.08mm/pixel$.

The mesh panel has been used to align the image with the ground line and to analyze the perspective error. The camera is centered to have a one point perspective, with the background tarps being perpendicular to the focal plane and the vanishing point in the center of the image. The perspective distortion has been determined by comparing the mesh panel point location with the linear fits expected from the magnification factor.

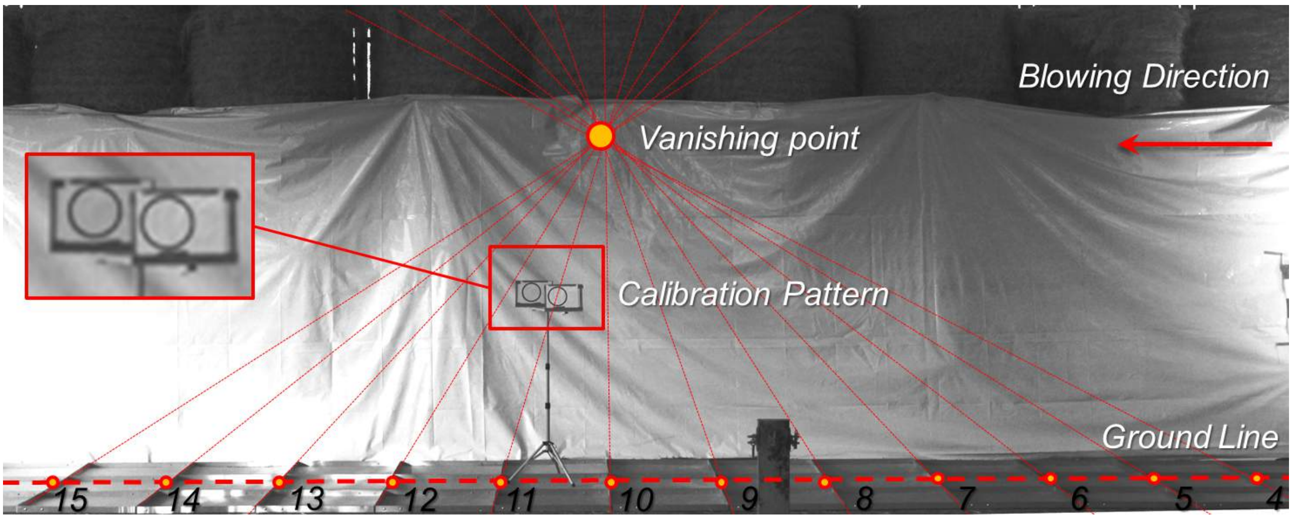

Fig. 2 Example of calibration image. The ground mesh panels gives the horizontal scale of the image, in meter. The vanishing point is approximately in the center of the image.

Fig.3 shows an example snapshot of the straw jet during the test. Depending on the light conditions, the image luminance in each straw elements range $10-20\%$ of the maximum value. The illumination of the scene is far from optimal: the background is unevenly illuminated and the tarp presents several wrinkles which reflects light in some regions and cast shadows in others. Depending on the light conditions, the image luminance in each straw elements range $10-20\%$ of the maximum value.

For each test, $n_t = 40$ images with $4272 \times 2848 pixels$ resolution, $16 bits$ depth, RGB images are acquired in multi-shooting mode at a $1 f.p.s.$ These images are flipped (left to right) to have the X axis direction from left to right.

Fig. 3 A typical snapshot image taken during the experiments. The background is dark in the center of the image, bright on the sides.

The straw jet is composed of a set of discrete straw packets, with a shape defined by the balance between aerodynamic forces, which tend to stretch and untie them, and particle-to-particle forces, which tend to keep them twisted. The purpose of our measurement technique is to detect the statistic boundaries of the straw packets and the average trajectory. The measurements are complemented, and validated, with the straw distribution at the ground, reconstructed by weighting the straw in each mesh panel at the end of the experiment.

The nozzle at the blower's outlet has a rectangular cross section of $40cm \times 20cm$ which can be either opened or closed at the bottom edge. To validate the method, this paper presents the results on four cases: two blower rotational speeds, namely $V_1 = 450 rpm$ and $V_2 = 540 rpm$, and two nozzle configurations, namely *Open* and *Closed* nozzles. In all the tests, the nozzle is tilted upward of $10°$ and the straw used is composed of node free wheat kernels.

3 Image Processing

This section presents the three steps of the image processing, which has been implemented in MATLAB 2015. The first step extracts straw elements using a K-means clustering in the *LaB* color space, as described in Sec.3.1. The second step removes the static objects using adaptive Eigenbackground subtraction, as described in Sec.3.2. The third step binarizes the average image with Otsu's method, extract and smooths its edges the resulting curves as described in Sec.3.3.

3.1 Color Segmentation: K-Means Clustering in *Lab* Color Space

Each of the $n_t = 40$ images is acquired in the RGB color-space, hence represented by a set of three matrices (R_i, G_i, B_i) of size $n_x \times n_y$ containing values in the range $[0, 1]$. For the example image in Fig.3, these components are shown in Fig.4.a. This color space has three limitations in segmentation analysis: it is brightness

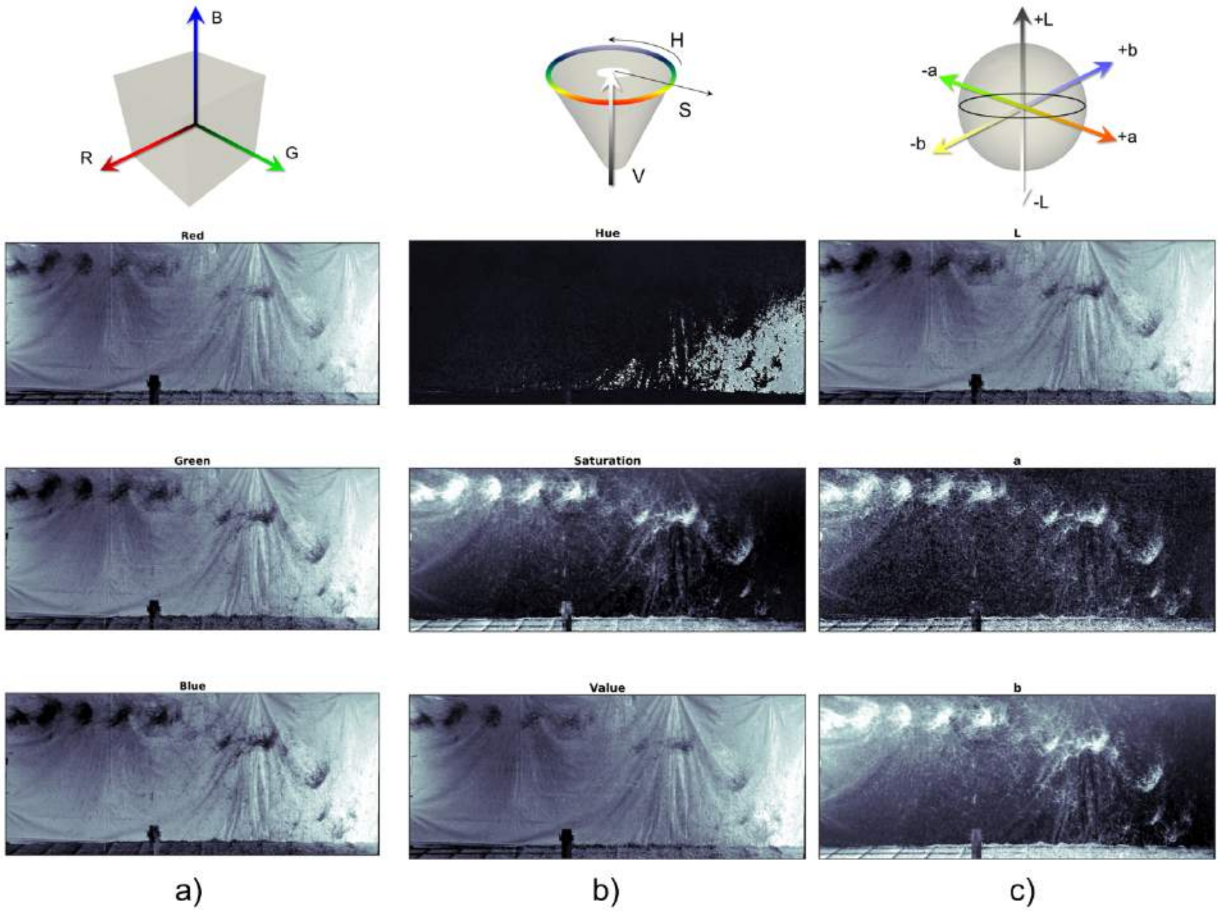

Fig. 4 *RGB* (a), *HSV* (b) and *Lab* (c) representation of the image snapshot in Fig.3, and spatial definition of their components. The histograms of all the images has been stretched to have 1% of the pixels saturated on both extremes.

dependent, meaning that a change in light intensity affects all its components; it is redundant, because its component are highly correlated; it is not provided with a linear color metrics, meaning that it not possible to measure color differences from their distance in this space.

The first two limitations are overcome by popular HS color-spaces such as *HSV*, *HSI* or *HSB*. In these spaces the color information, the *chrominance*, is expressed by two components: the Hue (H), which express the dominant wavelength of light and the Saturation (S), which express the amount of white mixed with the corresponding Hue (i.e. the color purity). The third component is assigned to light intensity, and each *HS* space uses a different combinations of *RGB* to compute it. For the example image shown in Fig.3, the *HSV* representation is in Fig.4.b. In uniform light conditions the saturation provides a highly contrasted monochrome image of the jet: the color of straw elements is far from white (i.e. it has high saturation) whereas the tarp is white (i.e. it has low saturation). In non optimal conditions, however, shadows and background defects also have high saturation and lead to over-segmentation of the straw jet. Moreover, the HSV space is affected by Hue ambiguity at low saturations and low values, as color is no longer distinguishable close to white or black.

Although the saturation channel is kept as the best grayscale representation of the images, the color segmentation proposed in this work benefits from a color-space provided of a linear metrics. This is the case of the CIElab, shortly referred to as *Lab*.

This space is derived from a non-linear transformation of the RGB intended to mimic the non linear response of human eye. It provides a color opponent representation in which, similarly to HS spaces, one component express the light intensity, (L) and two components express the color information: a and b contains the color coordinate in a green to red $(-a,a)$ and yellow to blue $(-b,b)$ axes. For the example image shown in Fig.3, these three components are shown in Fig.4.c. These two components do not have the *Hue* ambiguity problem and the color information in each of the $n_p = n_x n_y$ pixels is defined by a pairt $\mathbf{x}^{(i)} = (a_i, b_i)$, regardles of the light intensity L. Moreover, by construction, the set $\{\mathbf{x}^{(1)}, \mathbf{x}^{(2)} \dots \mathbf{x}^{(n_p)}\}$ spans a $\mathbb{R}^2$ space that is equipped with an Euclidean distance d_E. For the example Fig.3, this set is plotted in Fig.5.

This space is suited for k-means clustering, with the purpose of partitioning the pixel population into k clusters $\mathbb{S}_i$, each of which containing $|\mathbb{S}_i|$ elements, and so that $\sum_{i=0}^{k} |\mathbb{S}_i| = n_p$ and $\mathbb{S}_i \bigcap \mathbb{S}_j = 0 \, \forall i \neq j$. In its basic implementation [31] the number of cluster k is defined *a priori* so the classification problem is solved by minimizing the Euclidean distance d_e between an element $\mathbf{x}_i$ and the centroid μ_i of the cluster $\mathbb{S}_i$ to which it belongs:

$$min\left(\sum_{i=1}^{k}\sum_{x\in\mathbb{S}_i} d_e(\mathbf{x}_i,\mu_i)\right) = min\left(\sum_{i=1}^{k}\sum_{x\in\mathbb{S}_i} ||\mathbf{x}_i-\mu_i||^2\right) \qquad with \qquad \mu_i = \frac{1}{|\mathbb{S}_i|}\sum_{j\in\mathbb{S}_i}\mathbf{x}_j \quad \forall i \tag{1}$$

The algorithm start from a set of initial centroids μ_i, attributes the closest cluster to each element $\mathbf{x}_i$ and computes a new set of centroids on which it repeats the attribution element to cluster. In this work the number of cluster selected is $k = 4$. The resulting clusters are represented in Fig.5, then reshaped into images in Fig. 6.

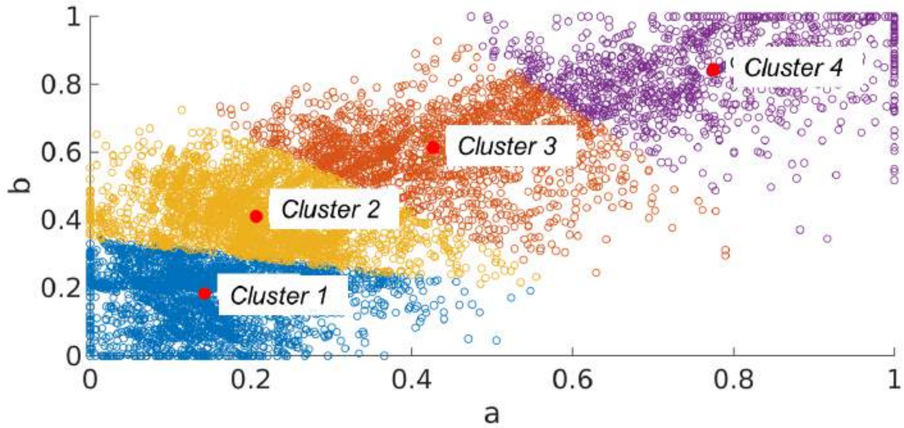

Fig. 5 Pixel color distribution in terms of color opponents $(a_i, b_i) \forall L$. For plottig purposes the only half of the pixel population is here represented.

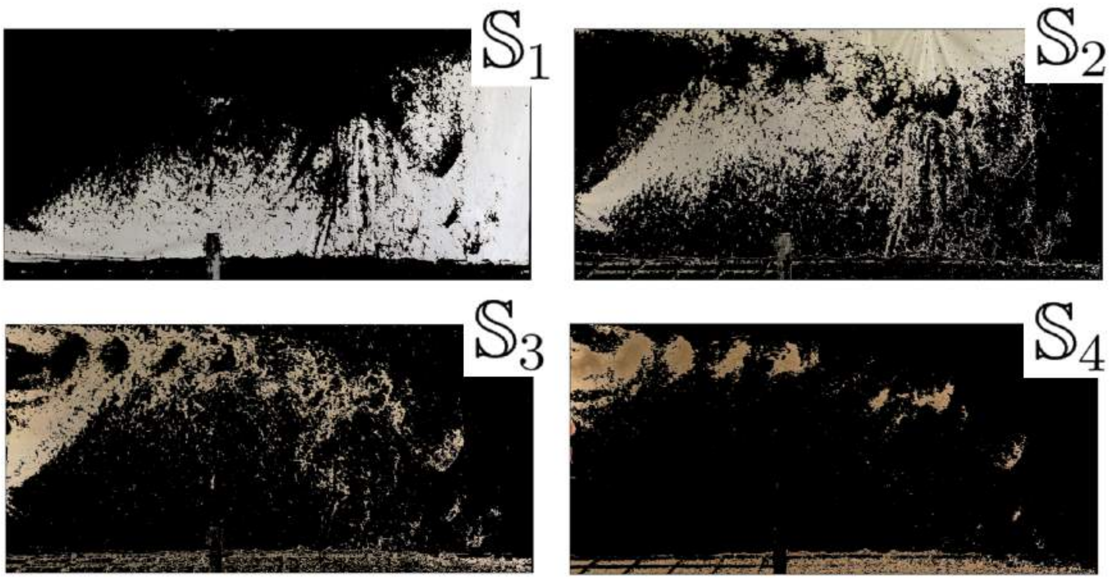

Fig. 6 Image Cluster Separation: the straw jet is the cluster with the highest saturation ($\mathbb{S}_4$), together with the straw on the ground and a small portion of the backgound remains. These parts are removed in the next step, the Eigen-Background.

At the end the operation, the cluster selected is the one having the centroid with the highest saturation, which is expressed by the modulus $S_i = \sqrt{a_i^2 + b_i^2}$. The resulting image is then converted to a monochrome image T_i taking its saturation component. For the example in Fig.3, the resulting T_i is shown in Fig.7.a.

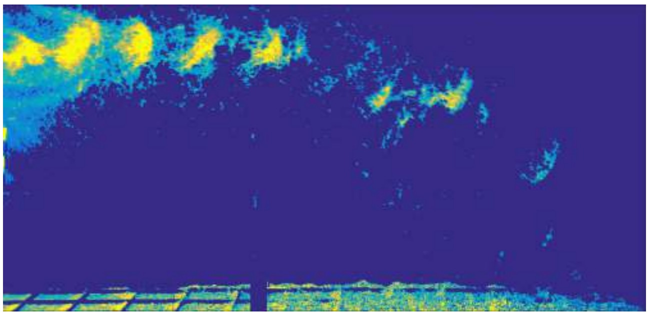

(a) Grayscale image T_i after color segmentation of Fig.3.

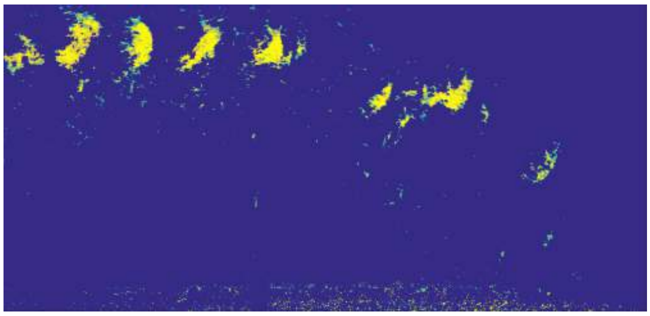

(b) Straw detection of Fig.3.

Fig. 7 Gray scale image T_i before (a) and after (b) the Eigen-Background subtraction.

3.2 Adaptive Background Subtraction: The Eigen-Background Decomposition

This step completes the segmentation removing static objects from the grayscale images T_i using Eigen-Background decomposition. First, each image $T_i \in \mathbb{R}^{n_x \times n_y}$ is reshaped into a column vector $I_i \in \mathbb{R}^{n_p \times 1}$. These n_t vectors become the $i-th$ column of a video matrix $A(n_p\,, n_t)$, after having removed the mean image:

$$A_{(n_s \times n_t)} = \begin{pmatrix} \hat{I}_1 & \hat{I}_2 & \cdots & \hat{I}_{n_t} \end{pmatrix} \quad with \quad \hat{I}_i = I_i - \frac{1}{n_t} \sum_{i=1}^{i=n_t} I_i \tag{2}$$

The columns of this matrix are usually independent, hence this matrix has a full rank $r = n_t$. However, because static objects appears in all the frames in the same position, their contribution to the information contained in the matrix has a much lower rank representation: a n_t set of images containing nothing but static objects, for example, can be represented by only one picture, i.e. one column of this matrix, i.e. a rank $r = 1$ representation.

The analysis of rank based decomposition–and approximation– of a matrix is known as Principal Component Analysis (PCA).The PCA can be obtained either by eigenvalue decomposition of the covariance[1] matrix $D = A^T \cdot A$, either by Singular Value Decomposition (SVD) of the matrix A. With the second approach, the video can be decomposed in its components E_k as follows:

$$A = \sum_0^{n_t} E_k = \sum_0^{n_t} \sigma_k u_k v_k \qquad with \qquad A = U\Sigma V^T = \begin{pmatrix} u_1 & u_2 & \cdots & u_{n_t} \end{pmatrix} \begin{pmatrix} \sigma_1 & 0 & \cdots & 0 \\ 0 & \sigma_2 & \cdots & 0 \\ 0 & 0 & \ddots & 0 \\ 0 & 0 & \cdots & \sigma_{n_t} \end{pmatrix} \begin{pmatrix} v_1 \\ v_2 \\ \vdots \\ v_{n_t} \end{pmatrix} \tag{3}$$

In the SVD decomposition: U is a $n_s \times n_t$ matrix whose columns u_k forms an orthonormal basis for the column space of A (hence the video frames); Σ is a $n_t \times n_t$ diagonal matrix, containing hight-to low ranked *singular values* σ_k in its diagonal; V^T is a $n_t \times n_t$ matrix whose raws v_k forms an orthonormal basis for the raw space of A (hence in the time domain). The key advantage of this decomposition is that components $E_k = \sigma_k u_k v_k$ are mutually orthogonal, meaning that $E_i \cdot E_j^T = 0\ \forall i \neq j$ and that the norm of each component is

[1]It is worth noticing that D is, by construction, square and symmetric. Therefore, its eigenvalue decomposition is $D = \Phi \Lambda \Phi^T$, with Λ the diagonal matrix containing the eigenvalues λ_i and Φ the matrix with the eigenvectors. Using the SVD in D reads: $D = A^T A = (U\Sigma V^T)^T (U\Sigma V^T) = (V\Sigma U^T)(U\Sigma V^T) = V\Sigma^2 V^T$, from which $\lambda_i = \sigma_i^2$. The technique was in fact named Eigen-Backgound because the PCA of the video matrix A was first presented in terms of λ_is.

defined by the singular value itself: $||E_k|| = \sigma_k$. This implies that the contribution to the matrix of each E_k is weighted by the singular value σ_k and the orthogonality guarantees that the error produced by taking only the first $p < n_t$ components is minimal, in a least square sense, and equal to the singular value of the first component left-out $||A - \sum_1^p E_k|| = \sigma_{p+1}$.

The n_t normalized singular values $\hat{\sigma}_j = \sigma_i/\sigma_1$ for a video sequence of T_i monochrome images are plotted in Fig. 8 for two cases: a) the gray scale are obtained from the raw saturation channel S of the images (Fig.4.b), b) the gray scale images T_i are obtained after the k-means color segmentation. It is worth noticing, in fact, that the less static objects appears in the video, the weaker is the singular value decay, meaning that more component are required to reproduce the information contained in A.

In this work we consider the first three components to be representative of the backgrounds, therefore we construct a video sequence $B = E_1 + E_2 + E_3$. The straw particle are detected, in in each frame, as the pixel regions from T_i which differ from the corresponding background of a given threshold Th. This threshold is fixed from the normalized singular value decay, selecting the contribution of the last ones, where the slope of the decay becomes negligible. Setting $Th = \hat{\sigma}(35)$ gives the result in Fig.7.b.

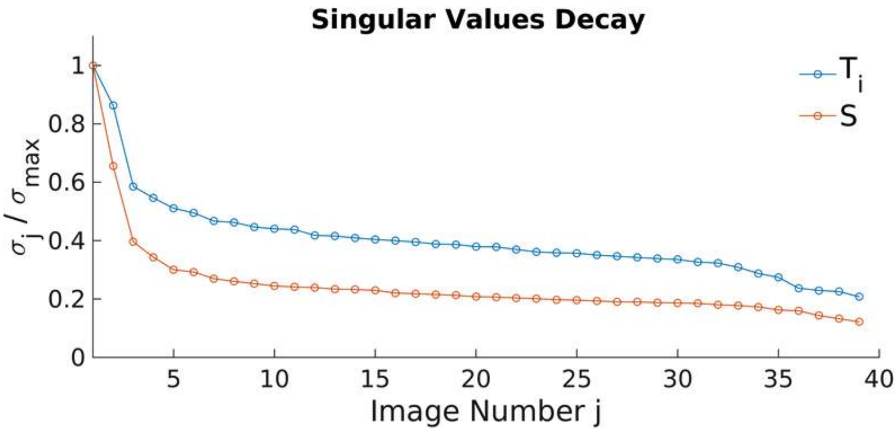

Fig. 8 Singular value decay for a video sequence before and after the color-space segmentation.

3.3 Geometrical Definition of Jet Trajectory and Spreading

After the color segmentation and the Eigen-Background subtraction, it is assumed that each video frame only contains straw element on a black background. From the set of $n_t = 40$ images, the average frame is shown in Fig.9.a. A standard Otsu's thresholding is used to compute its binary representation, and a morphology filter extracts only the connected area with the larger amount of pixels. This area is considered as the statistical average of the straw jet. Upper and lower edges are computed from a standard gradient method.The result is shown in Fig.9.b, with the calibration applied. These edges are smoothed using a 1-D moving average filter and fitted by a polynomial curve $f_B(x)$ and $f_T(x)$ respectively for the bottom and top edge.

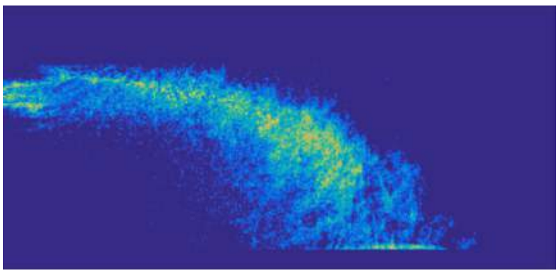

(a)

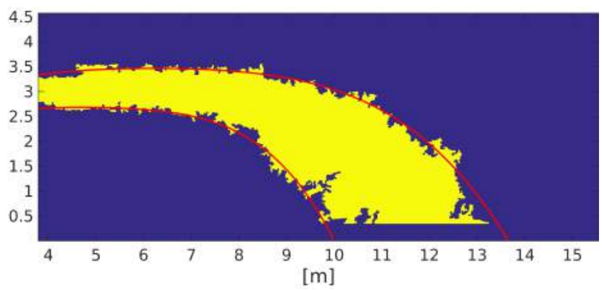

(b)

Fig. 9 Average image (a) and its binary image with smoothed edges (b).

These curves are the support for estimating the jet's geometrical centerline, trajectory and spreading. At the scope we define a discrete set of $n = 200$, Δx spaced points x_n. Along the two curves we consider the two polylines $f_B(x_n)$ and $f_T(x_n)$, having the same number of elements. Note that because of the different curve length, at this step it is necessary to let the bottom curve assume negative values. On a given point x_i, we define the jet width b_i as the local discrete Fréchet distance $b(x_i) = min\{d_E(f_B(x_i), f_T(x_n))\}$. The correspondent centerline $C_i = C(x_i)$ is then positioned so as to have an equal Fréchet distance from both the curves. The polyline connecting the discrete set of centerline points $C(x_n)$ is considered as the jet curvilinear trajectory ζ. The curvilinear length $\zeta(n)$ is finally computed as the sum of the chord lengths from 0 to n, i.e. $\zeta(n) = \sum_0^{n-1} \sqrt{\Delta x^2 + (C_{i+1} - C_i)^2}$. The geometrical construction for the example in Fig.9 is shown in Fig.10.

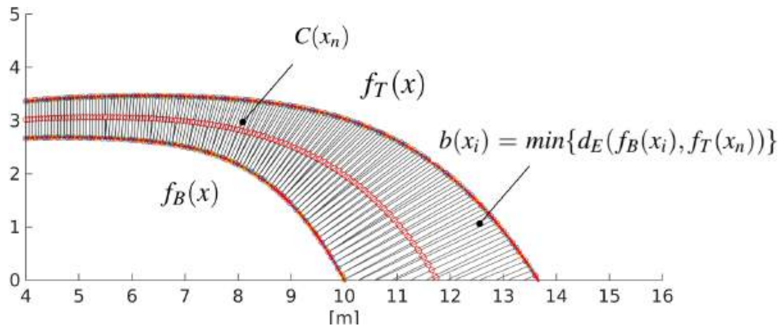

Fig. 10 Computation of Jet Trajectory and Spreading Binarized Edges.

4 Results and Discussion

In Fig.11 we compare the jet trajectory measurement for the open nozzle configuration at the two blower velocities; in Fig.12 we compare the weight distribution along the centerline axis and normalized with respect to the total mass distributed. Fig.13.a shows the centerline profile of the straw distribution at the ground, normalized to their respective maximum weights and Fig.13.b shows the jet spreading along curvilinear trajectory ζ.

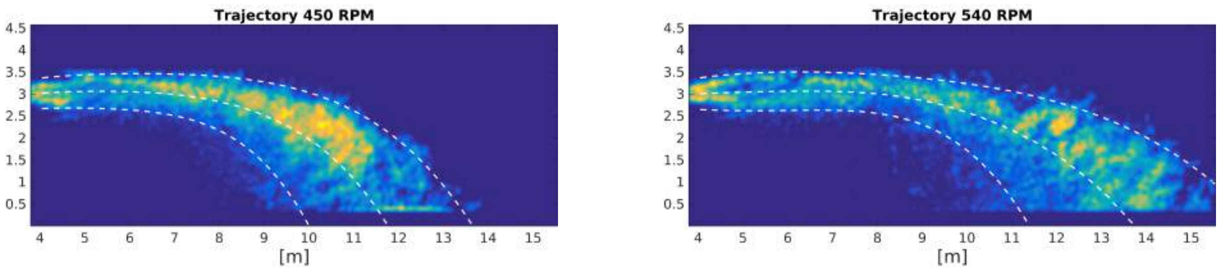

(a) $V_1 = 450rpm, Str_1$

(b) $V_2 = 540rpm, Str_1$

Fig. 11 Effect of blower velocity on open nozzle: measured trajectories and jet boundaries.

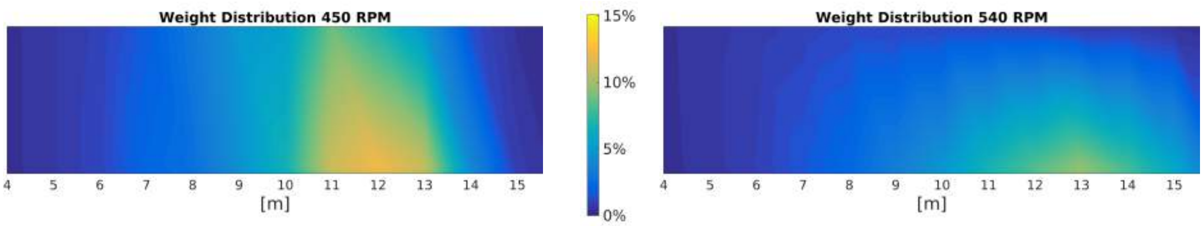

(a) $V_1 = 450rpm$

(b) $V_2 = 540rpm$

Fig. 12 Effect of blower velocity on open nozzle: interpolated, normalized, straw distribution on the ground mesh panels.

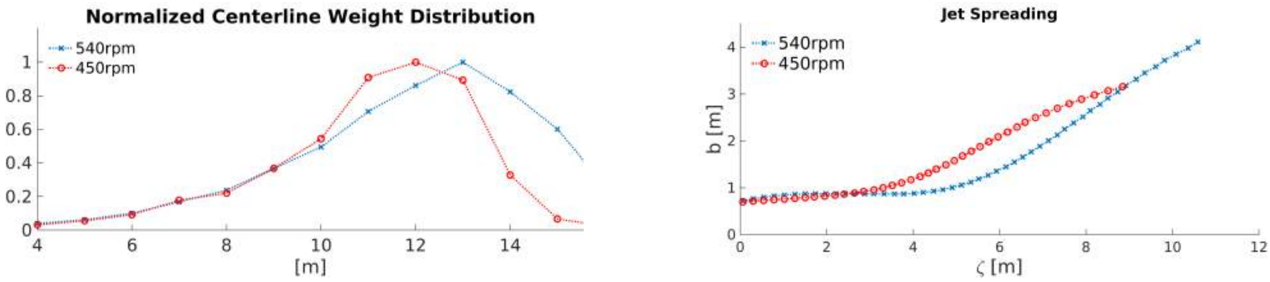

(a) Centerline Straw Distribution for $V1$ and $V2$

(b) Jet Spreading for $V1$ and $V2$

Fig. 13 Effect of blower velocity on open nozzle: centerline straw distribution at the ground and on jet spreading along the curvilinear trajectory ζ

Fig.11 shows that the jet remains horizontal and compact in a first phase, and starts spreading only in its descending phase. This is evident from Fig. 13.b, which shows a negligible jet spreading region followed by a linear spreading region along the curvilinear trajectory ζ. Increasing the blower velocity, i.e. the initial momentum of the straw, delays the spreading and descending phase of the jet.

It is observed that, although the jet is characterized by discrete packets of straw, twisted together along their entire trajectory, several straw particles lose detaches, and falls, when the jet centerline trajectory is still horizontal. These particles are removed by the image processing routine in its third step, the binarization, in which only the jet region is extracted. It is believed that they are responsible for the stream-wise skewness of the ground distribution in Fig.13.a, particularly its left tail. Noteworthy, these distributions are similar in this region: due to high particle-particle interaction (attractive, due to straw kernel twisting) the amount of particles leaving the jet boundaries is small and weakly affected by the blower velocity. In both tests, the location of the maximum weights on the ground agrees with the jet ranges $C(z=0)$ from the centerline trajectory.

For the closed nozzle case, the same results are collected in the Figs.14-16. A comparison with the previous figures shows that the jet is now more compact, with spreading rate almost halved with respect to the open nozzle. This is also evident in the straw distributions at the ground, where higher straw concentrations are reached and the relative importance of the left tail in the centerline straw distribution decreases. This suggest that a closer nozzle allows a better control of the straw casting, by forcing the conservation of horizontal momentum on a smaller jet cross-section. With respect to the open nozzle the ranges are slightly increases and, as before, the position of the maximum weight at the ground is correctly predicted from the trajectories.

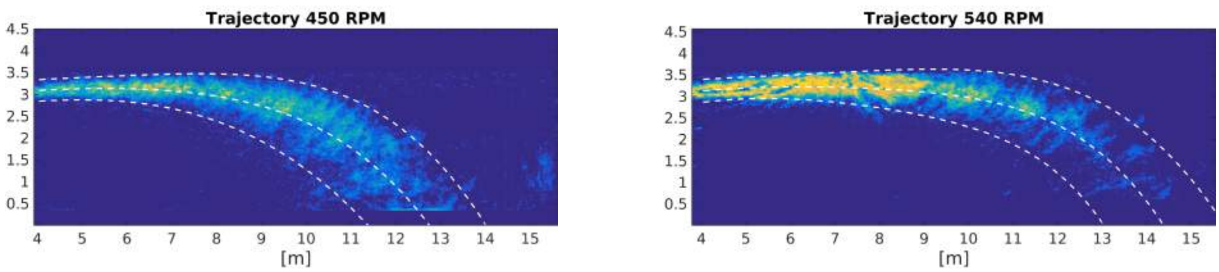

(a) $V_1 = 450rpm$

(b) $V_2 = 540rpm$

Fig. 14 Effect of Blower Velocity on closed nozzle: measured trajectories and jet boundaries.

5 Conclusions

This paper proposes a non invasive technique to measure the average trajectory and spreading of the particle-laden flow produced by straw blower machines. The method is based on an image processing routine to detect straw particles from a video sequence of the flow. The processing presented combines several techniques from computer vision and pattern recognition and proved to be sufficiently robust to work in daylight condition and

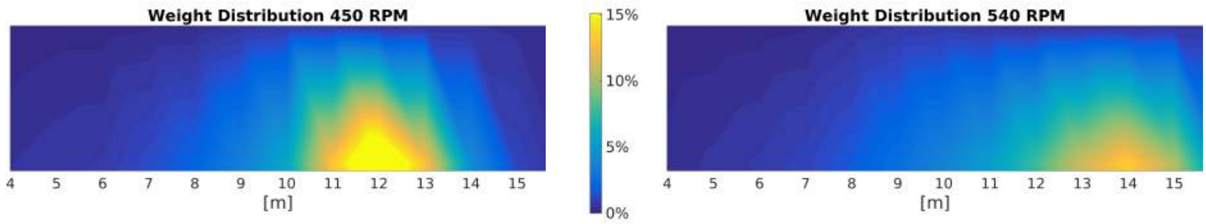

(a) $V_1 = 450rpm$ (b) $V_2 = 540rpm$

Fig. 15 Effect of blower velocity on closed nozzle: interpolated, normalized, straw distribution on the ground mesh panels.

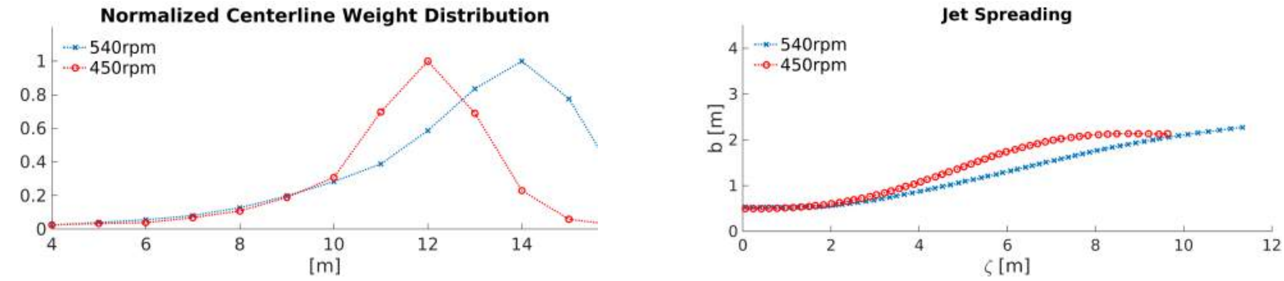

(a) Centerline Straw Distribution for $V1$ and $V2$ (b) Jet Spreading for $V1$ and $V2$

Fig. 16 Effect of Blower Velocity on closed Nozzle: interpolated, normalized, straw distribution on the ground mesh panels

unevenly illuminated scene. Using a simple set up– a tarp and a photo-camera on a podium– it was possible to have an insight on a complex flow. In particular, we compared two configurations for the blower's outlet nozzle: a closed nozzle, with a rectangular cross section, and an open nozzle, in which the bottom surface was removed. It was shown that a closed decreases the jet width, hence enhancing control and directionality of the final straw distribution.

Acknowledgments

M.A. Mendez is supported by a F.R.S.-FNRS FRIA grant. This project has been supported by the Centre Technique des Industries Mècaniques (CETIM). The experimental set up was prepared thanks to the close collaboration with the Kuhn Group in Copechagnière, France.

References

[1] Babcock, D. and R. A. McLaughlin (2008) Soil Facts – Mulch Options for Erosion Control on Construction Sites. N.S. State University

[2] New Hampshire Department of Environmental Services (2008) New Hampshire Stormwater Manual, Vol.1, Chapter 4.

[3] Storm Water Quality Handbooks (2003), Construction Site Best Management Practices Manual, *Straw Mulch*, Section 3, SS-6, Caltrans

[4] Tamburatzis,T., Pázsit (2013) Comparing Two-Phase Flow Regime Identification Approaches. In Rocha C. (ed) Artificial Intelligence and Hybrid Systems, iConcept Press Ltd. ISBN978-1-922227-065

[5] Brücker C. (2000) PIV in Two-Phase Flows. In: M.L. Riethmuller (ed) Particle Image Velocimetry and associated techniques, VKI-Lecture Series, Jan. 17-21

[6] Zimmer L. (2000) Particle tracking velocimetry and sizing in two-phase flows. In:M.L. Riethmuller (ed) Particle Image Velocimetry and associated techniques, VKI-Lecture Series, Jan. 17-21

[7] Lee, T.-W. (2008) Flow Visualization and Image Analysis. In: T.-W. Lee (ed) Thermal and Flow Measurements. CRC Press, pp 89-124, ISBN 9780849379703

[8] Antonio Busciglio, Giuseppa Vella and Giorgio Micale (2012). Measurement of Multiphase Flow Characteristics Via Image Analysis Techniques: The Fluidization Case Study. In: Jin - Hai Zheng (ed.) Hydrodynamics - Theory and Model, doi: 10.5772/28376.

[9] F. Tomasoni, H. van Parys, H. Terryn, A. Hubin, J. Deconinck, J.M. Buchlin, J. van Beeck (2010) Identification of bubble evolution mechanisms during AC electrograining *Electrochemistry Communications*, vol. 12, No.1, pp 156-159. , doi:10.1016/j.elecom.2009.11.012

[10] F. Tomasoni, J. van Beeck and M. Riethmuller (2010). Experimental determination of bubble-flow interaction at gas evolving electrode. In: Proceeding of the 15th In. Symp on Applications of Laser Techniques to Fluid Mechanics, Lisbon, Portugal, 05-08 July, 2010

[11] Akhmetbekov, Y. , Alekseenko, S.V., Dulin, V.M., Markovich, D. M., Pervunin, K. S. (2010). Planar fluorescence for round bubble imaging and its application for the study of an axisymmetric two-phase jet *Experiments in Fluids*, vol. 48, No.4, pp 615-629, doi:10.1007/s00348-009-0797-0.

[12] R.Pal,N. and Bhandari,D. (1993) Image Thresholding: Some new techniques. *Signal Processing*, vol. 33, pp 139-158. , Elsevier, doi:10.1016/0165-1684(93)90107-L

[13] Nikhil R Pal, Sankar K Pal (1993) A review on Image Segmentation Techniques *Pattern Recognition*, vol. 26, No.9, pp 1277-1293. , doi:10.1016/0031-3203(93)90135-J

[14] Yang X., Beyenal H., Harkin G., Lewandowski Z. (2001) Evaluation of Biofilm Image Thresholding Methods *Water Research*, vol. 35, No.5, pp 1149-1158, doi: 10.1016/S0043-1354(00)00361-4

[15] Planquart, P., Riethmuller, M., Joly, A., Detry, J. M., (2002). Real time optical detection and characterisation of water model free surfaces– Application to the study of the mold. In: Proceeding of the 4th European Continuous Casting Conference, Birmingham, UK.

[16] Tóth,B., Anthoine,J., Riethmuller, M.L., (2006). Dynamic measurements of the shape of a free surface. (In French language) In: Proceeding of the 9th Congrús Francophone de Techniques Laser, Toulouse, France, 2006.

[17] Tóth,B., (2008). Two-phase flow investigation in a cold-gas solid rocket motor model throught the study of the slag accumulation process. Ph.D. thesis, Université libre de Bruxelles, Brussels, Belgium.

[18] Sanchis, A. and Jensen, A. (2011) Dynamic masking of PIV images using the Radon transform in free surface flows. *Experiments in Fluids*, vol. 51, n.4, pp 871-880. doi: 10.1007/s00348-011-1101-7

[19] Murphy, L. M. (1986) Linear feature detection and enhancement in noisy images via the radon transform *Pattern Recognition Lett*, vol. 4, pp 279-284. doi:10.1016/0167-8655(86)90009-7

[20] Cheng, H.D, Jian, X.H., Sun,Y., Wang,J. (2001) Color Segmentation: advances and prospects, *Pattern Recognition*, vol.34, n.12, pp 2259-2281. doi:10.1016/S0031-3203(00)00149-7

[21] Skarbek. W, Koschan.A, (1994) Colour Image Segmentation - A Survey - Technical Report 94-32, Tech. Yniv. Of Berlin, October 1994.

[22] Shamik, S., Gang, Q.and Sakti, P. (2002) Segmentation and Histogram Generation Using the HSV Color Space for Image Retrieval. In: International Conference on Image Processing (ICIP), pp 589-592.

[23] Grundland. M, Dodgson N.A, (2007) Decolorize: Fast, Contrast Enhancing, Color to Grayscale Conversion *Pattern Recognition*, vol. 40, n. 11, pp 2891-2896 ISSN 0031-3203

[24] Pappas, T. (1992) An adaptive clustering algorithm for image segmentation *IEEE Trans. Signal Process*, vol. 40, n. 4, pp 901-914 doi: 10.1109/78.127962

[25] Comaniciu. D., Meer P., (2002) Mean Shift: A robust approach toward feature space analysis *IEEE Trans. Pattern Analysis Machine Intell*, vol. 24, n. 5, pp 603-619 doi:10.1109/34.1000236

[26] Baldevbhai. P.J., Anand R.S, (2012) Color Image Segmentation for Medical Images using La^*b^* Color Space *Journal of Electronics and Communication Engineering*, vol. 1, n. 2, pp 24-45 ISSN 2278-2834

[27] Bansal S., Aggarwal D., (2011) Color Image Segmentation using CIELab Color Space using Ant Colony Optimization *International Journal of Computer Applications*, vol. 29, n. 9, pp 28-34 doi:10.5120/3590-4978

[28] Picardi, M. (2004). Background subtraction techniques – a review. In: International Conference on Systems, man and cybernetics, ICSMC - 04, pp 3099-3104.

[29] Sobral,A. and Vacavant, A. (2014). A comprehensive review of background subtraction algorithms evaluated with synthetic and real videos *Computer Vision and Image Understanding*, vol. 122, pp 4-21. doi:10.1016/j.cviu.2013.12.005

[30] Oliver, N.M. and Rosario, B. and Pentland, A.P. (2000). A Bayesian computer vision system for modeling human interactions *Pattern Analysis and Machine Intelligence, IEEE Transactions on*, vol. 22, n.8 ,pp 831-843. doi:10.1109/34.868684

[31] Lloyd, Stuart P. (1982), Least squares quantization in PCM, *IEEE Transactions on Information Theory*, vol 28 n 2 pp 129-137, doi:10.1109/TIT.1982.1056489.